

# Machine-Learning Interatomic Potential for Twisted Hexagonal Boron Nitride: Accurate Structural Relaxation and Emergent Polarization

Wilson Nieto Luna,\* Robin Smeyers, Lucian Covaci, Cem Sevik, and Milorad V. Milošević

*Department of Physics and NANOLight Center of Excellence,  
University of Antwerp, Groenenborgerlaan 171, 2020 Antwerp, Belgium*

(Dated: March 18, 2025)

The emerging ferroelectric properties of two-dimensional (2D) heterostructures are at the forefront of science and prospective technology. In moiré bilayers, twisting or heterostructuring causes local atomic reconstruction, which even at picometer scale, can lead to pronounced ferroelectric polarization. Accurately determining this reconstruction utilizing ab initio methods is unfeasible for the relevant system sizes, but modern machine-learning interatomic potentials offer a viable solution. Here, we present the Gaussian Approximation Potential for twisted hexagonal boron nitride (hBN) layers validated against ab initio datasets. This approach enables the precise analysis of their structural properties, which is particularly relevant at small twist angles. We couple the structural information to a tight-binding model based on accurate interatomic positioning, and determine the twist-dependent polarization, yielding results that closely align with previous experimental findings - even at room temperature. This methodology enables further studies that are unattainable otherwise and is transferable to other 2D materials of interest.

Ferroelectric materials exhibit spontaneous electric polarization that can be controlled by an external electric field. This polarization originates from a symmetry-breaking structural phase transition, leading to a spontaneous alignment of electric dipoles that gives rise to a macroscopic polarization [1–3]. Research on controlling ferroelectricity has advanced rapidly in recent years due to its relevance in diverse fields including electronics [4], telecommunications [5], and energy-related applications [6]. Traditional approaches, such as thinning bulk oxide ferroelectrics [7], have proven to be challenging. However, the emergence of two-dimensional (2D) materials and their van der Waals (vdW) heterostructures offers a feasible alternative for designing ferroelectrics with added versatility. Specifically, properties that are highly sensitive to strain [8, 9], bending [10], stacking order [11], and interlayer twisting [12] are highly relevant for ferroelectric properties. Furthermore, vdW materials can be integrated with existing metal-oxide semiconductor technology [13], making them promising candidates for post-Moore’s law nanoelectronics.

Intrinsic ferroelectricity in vdW materials is scarce because it requires the material’s bulk crystal to belong to a polar space group [14]. Furthermore, multilayer vdW crystals, such as graphene or hexagonal boron nitride (*h*-BN), tend to form stable centrosymmetric stacking configurations, naturally excluding ferroelectricity. To overcome this drawback, potential vdW ferroelectrics have been engineered by introducing a twist between layers, thereby breaking the central symmetry of the heterostructure [15]. Recent experiments have validated this concept by revealing highly polarized domains in twisted *h*-BN[15], revealing a crucial building block for high-density, non-volatile memory applications [16]. Subsequent experiments have expanded this approach, driven

not only by the potential of twisted 2D materials to act as novel polarized materials but also by the unique functionality provided by periodic polarization patterns. These patterns create tunable spatially varying electrostatic potentials, which can dynamically modulate the electronic[17], optical[18], and magnetic properties of adjacent 2D materials. Such capabilities open new avenues for engineering quantum phenomena – including charge density wave manipulation[19] or exciton trapping[20–22] – in tailored two-dimensional heterostructures.

A comprehensive computational investigation of these fundamentally and technologically promising features is essential; however, it is complicated due to the large-scale periodicity inherent in twisted structures, which prevents atomic relaxation at the first-principles level. Whereas, precise polarization characterization requires highly accurate alignment of the out-of-plane distances among atoms constituting layers. Empirical potentials offer a partial solution for computational cost, but the accuracy level for precise polarization prediction is highly questionable. However, a state-of-the-art class of potentials based on machine learning (ML) methodologies has recently emerged, advancing the accuracy of energy and force up to the first-principles levels.

Kernel-based ML potentials[23] describe the potential energy surface (PES) of a system as a sum of local environments, ensuring invariance to translation, rotation, and permutation of atoms[24]. In this framework, Gaussian Approximation Potentials (GAP), [25, 26], apply Gaussian process regression to interpolate the PES, making them a robust tool for accurately predicting atomic energies and forces. This methodology has demonstrated success in modeling the properties of materials such as silicon, gold, and carbon[27], and has shown promising results in systems like graphene[28] and hexagonal boron nitride (hBN)[29, 30].

Considering these aspects, to identify the polarization in twisted *h*-BN heterobilayer crystals, we first devel-

\* [wilson.nieto@uantwerpen.be](mailto:wilson.nieto@uantwerpen.be)

oped a GAP-based machine learning model to capture interatomic forces with first-principles accuracy, addressing both in-plane and out-of-plane interactions. Subsequently, using a tight-binding (TB) approach, we calculated the intrinsic polarization of twisted  $h$ -BN crystals. The results demonstrate that the complete relaxation of ions in twisted layers significantly influences the final polarization values, and that an accurate representation of atomic positions in these layers yields excellent agreement with experimental predictions.

We start by constructing the ML potential for twisted  $h$ -BN in order to tackle the problem of atomic relaxation in this type of structures. To construct an accurate database, we followed a similar procedure as the one described in [28], in which we build the training configuration with an iterative approach. Training configurations were obtained from first-principles calculations on twisted structures with angles  $\theta$  between  $21.75^\circ$  and  $7.34^\circ$ , based on DFT as implemented by the Vienna Ab initio Simulation Package (VASP) [31, 32]. With a reliable database, we can build an accurate interatomic potential based on the DFT energies and forces. From this potential we can predict structural properties of smaller twist angles that were not included in the training configurations. A more detailed explanation about the training configuration is presented in the Supporting Information. The main indication of the quality of the potential is the quality of the forces it predicts compared to a proper reference. In our case we will compare forces predicted by our model in the validation set to the original values obtained from a DFT calculation. This is shown in fig.1.a, we can see the correlation between forces predicted by the GAP model and the DFT calculation align very closely, with the errors being presented in fig.1.c. We divide the forces into the out-of-plane and in-plane component, shown in red and black respectively in fig.1.a-d. The forces were obtained with an RMSE of  $0.012 \text{ eV } \text{\AA}^{-1}$  in the out-of-plane direction, and  $0.019 \text{ eV } \text{\AA}^{-1}$  in the in-plane direction, where the errors follow a Gaussian distribution as expected. In figure 1.b we show the same force correlation and distribution of errors for the Tersoff[33–35] potential in combination with the ILP potential [36], the current state of the art classical potential used for this type of system. Our model shows a significant improvement in the prediction of the interlayer interaction, offering an improvement of about one order of magnitude in the prediction of forces. In fig.1.e-f we present the correlation between the predicted forces of our GAP potential and the DFT forces for a bilayer system with 1% uniaxial strain in the  $y$ -axis, and we also compare the energy predicted by DFT and GAP methods. Although these types of systems were not included in the training configuration, the twisted structures present intrinsic strain that was captured by the GAP potential and it is able to predict the forces and energy, as shown in the correlation plot, with an RMSE of  $0.24 \text{ eV } \text{\AA}^{-1}$  and  $0.011 \text{ eV/atom}$  respectively. This accuracy can be improved by including strained structures in our training set.

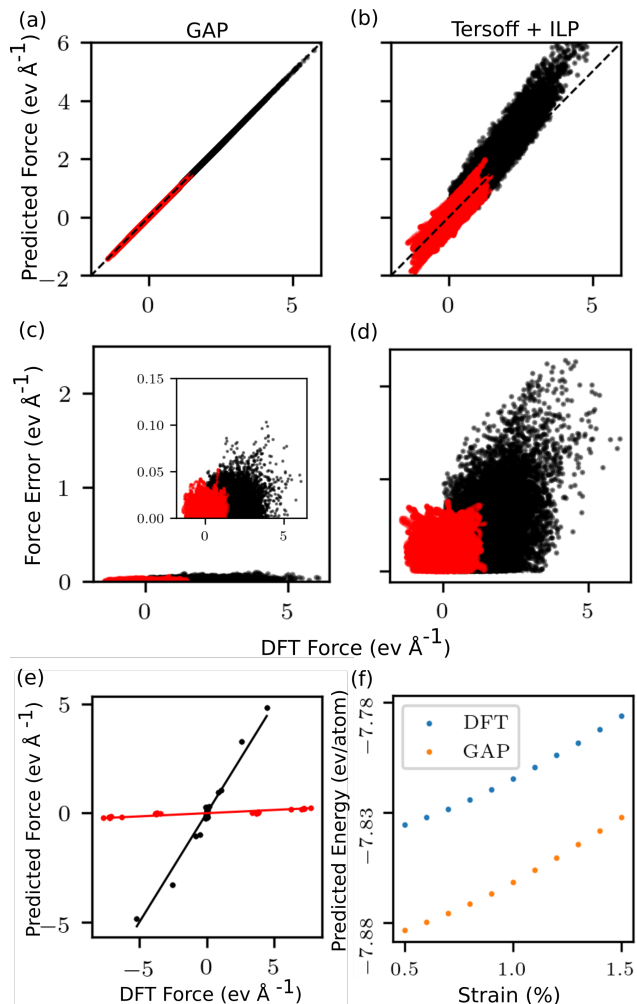


Figure 1. (a) Force correlation plot for twisted  $h$ -BN using the GAP potential. (b) Force correlation plot for twisted  $h$ -BN using the classical potentials. (c) Error distribution for the GAP potential, the inset shows a zoom in view of the distribution of the errors. (d) Error distribution for the classical potential. (e) Force correlation plot for a twisted system of  $h$ -BN with 1% uniaxial strain. (f) Comparison of predicted energy between ab-initio methods and our model for different values of strain. In all the pictures, red dots indicate out-of-plane forces and black dots indicate in-plane forces.

Next, we calculate the structural properties of twisted  $h$ -BN, for which the results are presented in figures 2 and 3. The primary descriptor for studying the structural properties is the interlayer distance, defined in this work as the average distance in the  $z$ -direction between each atom and its 3 nearest neighbors in the opposite layer. Since atoms in both layers do not necessarily overlap, an interpolation was applied to have a continuous description of the interlayer distance, shown in fig.2.b, from which we extract the moiré unit cell. We can clearly observe four different regimes: moiré ( $\theta > 13.17^\circ$ ), transition ( $5.09^\circ < \theta < 13.17^\circ$ ), soliton ( $1.89^\circ < \theta < 5.09^\circ$ ), and domain-soliton ( $\theta < 1.89^\circ$ ) regimes[37]. In the moiré

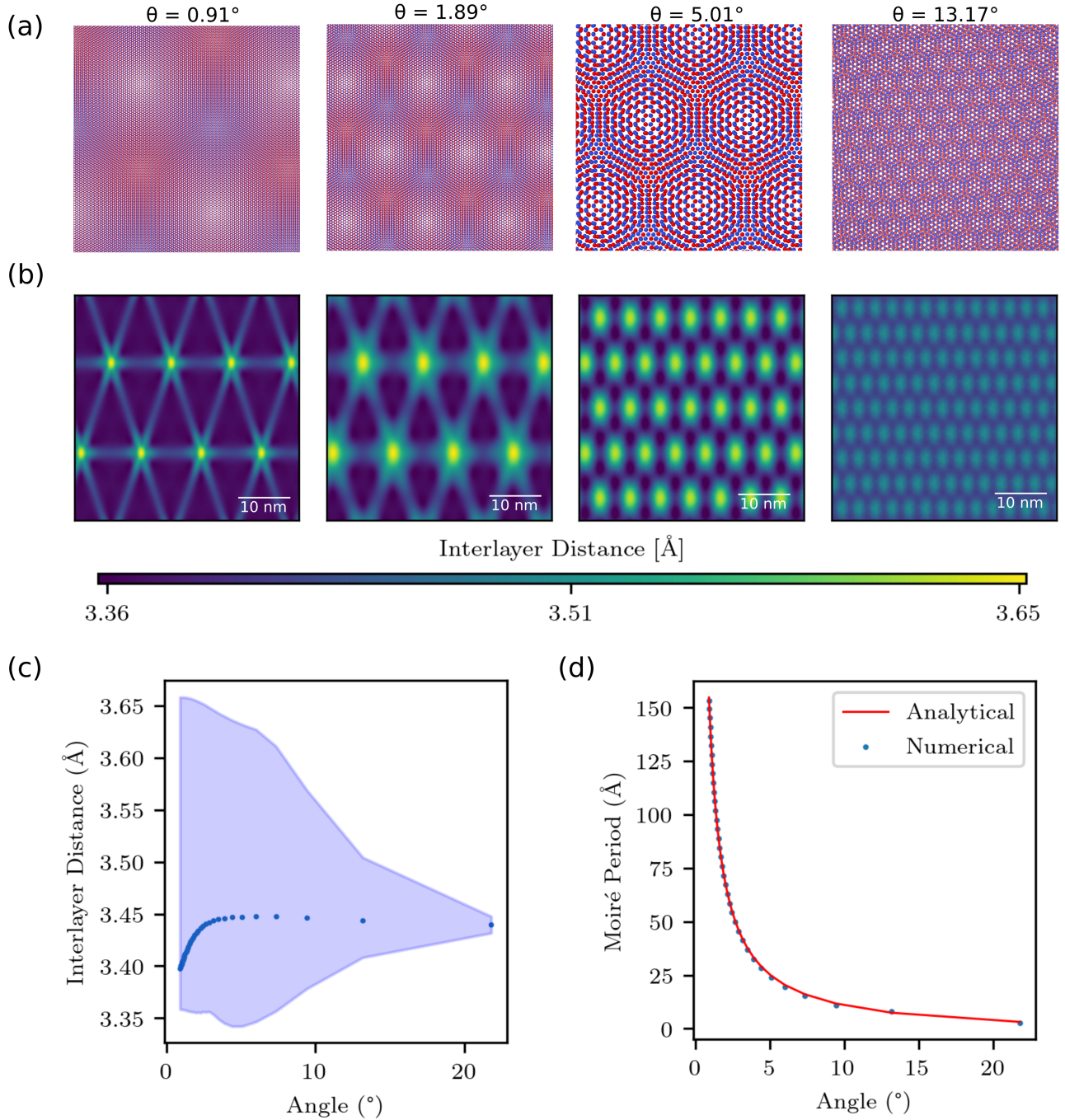


Figure 2. Different structures with corresponding  $\theta$  for different regimes in twisted bilayer hBN. (a) Top view of the relaxed lattice with B atoms in red and N atoms in blue. (b) Interlayer distance landscape, calculated from the atoms in the top layer. (c)  $d_{max}$ ,  $d_{min}$  and  $\langle d \rangle$  as a function of the twist angle. The blue dots represent  $\langle d \rangle$  and the blue shade represents the interval between  $d_{max}$  and  $d_{min}$ . (d) Moiré period as a function of the twist angle.

regime we can model the twisted structures as rigidly twisted because the variation in interlayer distance becomes negligible. In the transition regime, relaxation effects become more important and some structural characteristics start to appear; the system starts going through a continuous transition into the soliton regime. In the

soliton regime, solitons appear as bridges between nodes, and as borders for stacking domains. These stacking domains form a honeycomb lattice but are still small in comparison with the size of the nodes. When going further in decreasing  $\theta$  we enter the domain-soliton regime, the stacking domains become dominant along the struc-

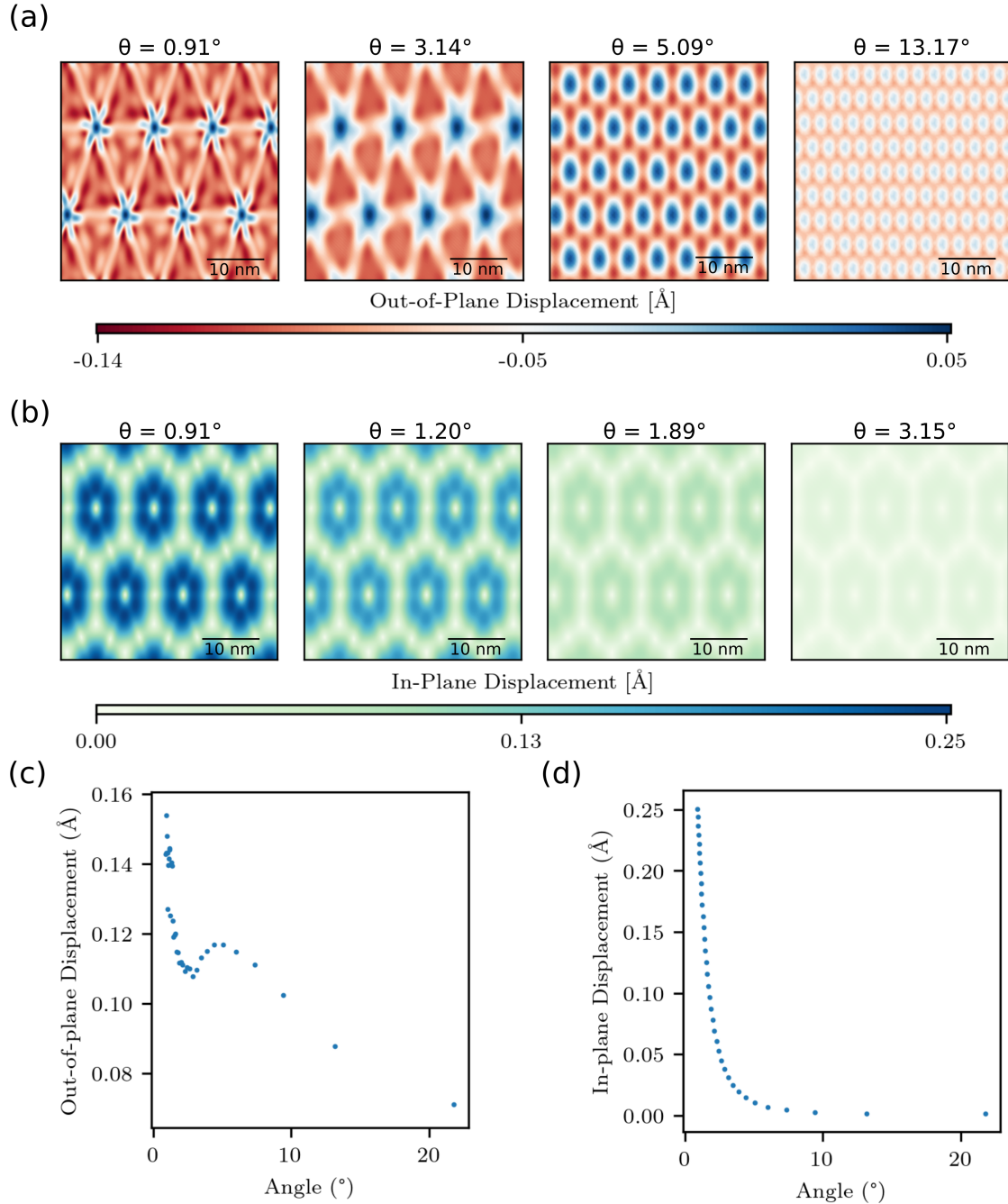


Figure 3. (a) Out-of-plane displacement map for four different twist angles after relaxation. (b) In-plane displacement map for four different twist angles after relaxation. (c) Maximum value of the out-of-plane displacement as a function of  $\theta$ . (d) Maximum value of the in-plane displacement, since some displacements are negative, the absolute value of this quantity is shown. In (a) and (b) only the view of the top layer is shown.

ture forming a hexagonal network with the nodes at the intersection points. In fig.2.c we can see the distribution of the interlayer distance as a function of the twist angle, with the dots representing the mean interlayer distance across the moiré unit cell, and the shaded region representing the interval between the maximum and the minimum interlayer distance. As we can see from the plot, the

rigid twist approximation is valid at large twist angles, as the variation in interlayer distance becomes progressively smaller. We can see a steep decrease in  $\langle d \rangle$ , meaning the stacking domains become dominant, so we can associate this steep decrease as the shift from the transition regime to the soliton one. Similarly, in fig.2.d, we show the moiré periodicity  $a_m$ , which is obtained numerically from the

interlayer distance landscape using our GAP model (blue dots) and compared to the analytical prediction (red line) [38]. We obtain an excellent match between both, further validating the accuracy of our model.

We continue by analyzing the atomic displacements in structurally relaxed twisted layers of *h*-BN. The color map of the out-of-plane and in-plane displacements can be seen in fig.3.a and b respectively. The maximum value of each displacement as a function of  $\theta$  are shown in fig.3.c-d. From these graphs, we can see that in the moiré regime there is no atomic reconstruction, since both in- and out-of-plane displacements are negligible. In the transition regime, the out-of-plane displacement gains relevance, but the in-plane displacement is still negligible. The in-plane displacement becomes significant with emerging solitons, while the out-of-plane displacement mirrors the interlayer distance landscape, peaking where the interlayer distance nodes appear. The small increase in the out-of-plane distance maximum at around  $5^\circ$ , we attribute to a change of regime and is also in accordance with an increase in the interlayer distance interval, shown in fig.2.c.

Before discussing the polarization of twisted *h*-BN structures, it is essential to understand the origin of ferroelectricity and the resulting macroscopic polarization in these type of structures. The symmetry-breaking structural phase transition leads to the ordered arrangement of electric dipoles, resulting in spontaneous polarization that contributes to macroscopic polarization[1]. Ferroelectricity spontaneously appears in twisted layers of *h*-BN from the overlap of B and N atoms, and the distortion of the  $p_z$  orbitals of each atom. In previous work, it is shown that ferroelectricity is completely dictated by the commensurability of the system [39]. The AB/BA stacking configuration becomes dominant, hence maximizing the overlap of B and N atoms. We expect that in AB/BA stacking regions a spontaneous polarization emerges from the system. From the structural analysis of the system we see that AB/BA stacking regions become dominant after relaxation and at small  $\theta$ . There are several approaches to calculate the polarization of a system, ranging from the Berry Phase method[40] to an approach in which we calculate the local density of states to obtain the charge distribution around the system, from which the electrostatic potential is obtained. We opt for the latter approach, since it is computationally cheaper while maintaining a high level of accuracy.

We set up a tight-binding model based on relative interatomic positioning that has proven valid in similar systems[42, 43]. We used Pybinding [44], a Python package, to set up and solve the tight-binding model, relying on the KPM method [45] in order to obtain the electronic local density of states. For a more detailed description about the tight-binding model and the details about the calculation, we refer the reader to the Supplemental Information.

Experiments on twisted *h*-BN suggest that there is an electric potential pattern arising from the structure[41].

We calculate the induced charge density distribution after twist by summing over all occupied states up to the charge neutrality point. As can be seen in fig.4.b, the relaxation emphasizes the triangular pattern that can be observed in experiments. Most of the induced charge is carried by B atoms, with the induced charge being  $\sim 3$  times larger than that of N atoms. In the soliton and domain-soliton regimes, the twist angle has the effect of increasing the size of the charged domains, but has no significant effect in the value of the electron density of the domains. The calculated electron density is on the order of  $10^{12} \text{cm}^{-2}$ , which is in accordance with previous theoretical results [46].

As mentioned above, twist induces an electrostatic potential at the surface of the *h*-BN top layer caused by the differential charge redistribution  $\Delta\sigma$ . This charge redistribution induces an electric polarization at the buried interface. Crystals of *h*-BN are naturally stacked in an AA' sequence, but in order to generate this polarization, the system prefers a more energetically favorable stacking configuration, AB/BA. The electrostatic potential is shown in fig.4.a, we can see that, similar to the charge redistribution, the electrostatic potential also has a triangular symmetry, and becomes neutral in regions of AA stacking as expected. The magnitude of the electrostatic potential also increases as the twist angle decreases, we attribute this to the increase in the size of the AB/BA domains, hence there is more twist-induced charge.

The out-of-plane polarization of the system can be calculated following the procedure of [22]. At close distance from the *h*BN Milorad Milosevic interface we can define the electrical polarization as  $P_{max} = \epsilon_0(V_{max} - V_{min})$ , where  $P_{max}$  is the electrical out-of-plane polarization at the AB stacking configuration, and the difference in the electrostatic potential is the potential drop when going from an AB stacking configuration to BA. In fig.4.c we can observe the value of the polarization as a function of  $\theta$ . Our results are in perfect agreement with previous experimental works[41], validating our methodology. As expected, the polarization is inversely proportional to  $\theta$  because the size of the stacking domains follows the same trend which increases the amount of charge redistribution, thus giving a greater contribution to the polarization. We also see that atomic relaxation of the system enhances the out-of-plane polarization. In a previous theoretical work[47] in which the out-of-plane polarization of bilayer *h*BN is calculated in the AB stacking, a value of  $2 \text{ [pC/m]}$  is obtained. This is also the upper bound value we find for our calculations as we can see in fig.4.d. We also analyze the effect of temperature by repeating our calculation for systems that underwent a molecular dynamics run at temperatures 100 K, 200 K, 300 K, which are also included in our training set (see Supporting Information). The magnitude of the polarization remains unchanged at these temperatures, but as shown in fig.4.a the shape of the domains changes drastically. To analyze the MD at finite temperature, we ran the simulation for 30 ps and then did a statistical average with every step.

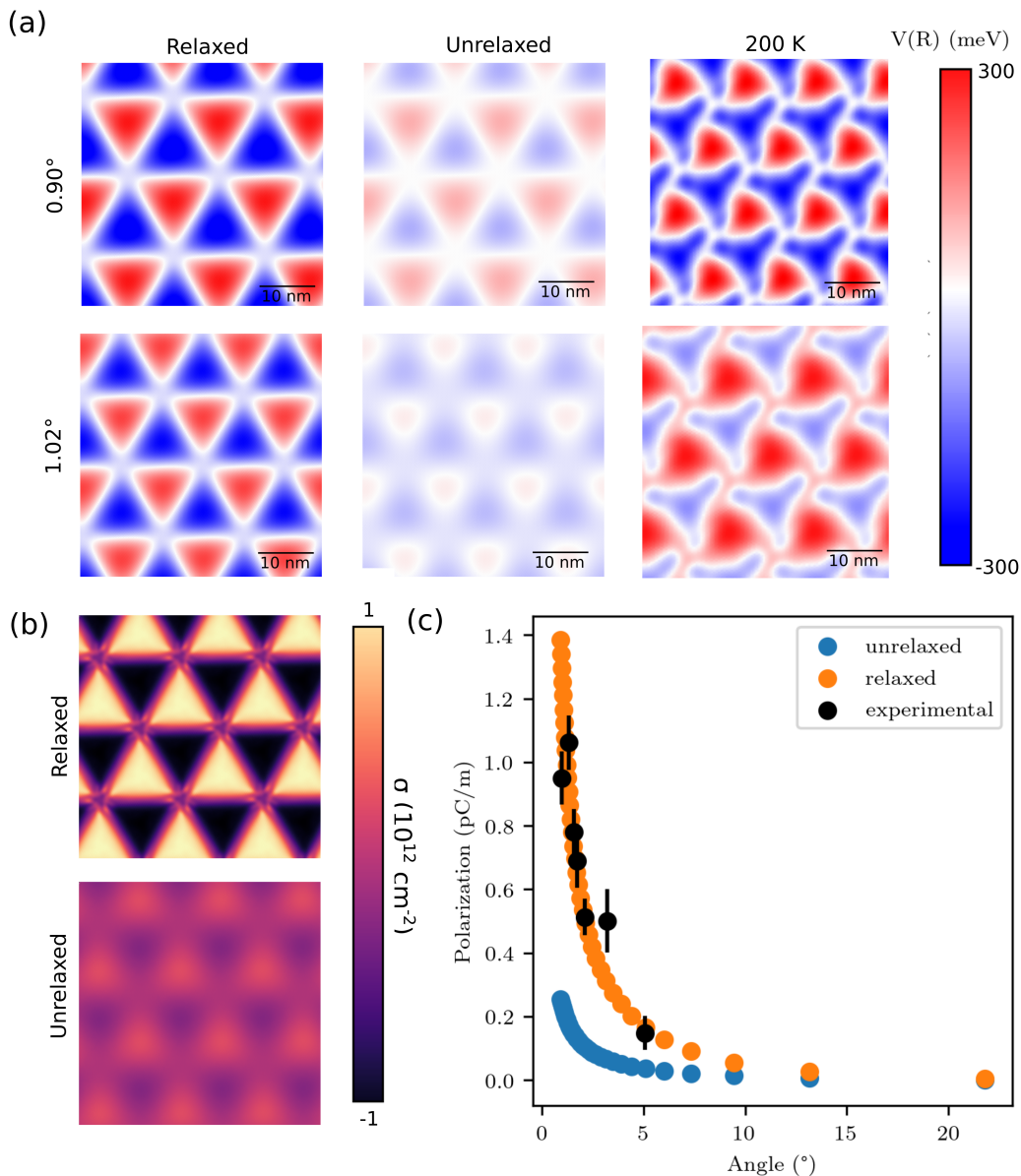


Figure 4. (a) Coulomb potential for two different twist angles, before and after relaxation, and after a MD run at 200 K. Only the top layer is shown. (b) Charge redistribution for a relaxed and a hard twist of the layers. The colorbar is in units of  $10^{12} \text{ e cm}^{-2}$ . (c)  $P_{max}$  as a function of  $\theta$ . The black dots represent experimental data with their corresponding errorbar obtained from [41].

We fixed the AA stacking nodes and proceeded with the average; we account for the change in the shape of domains to this pinning and the AB/BA regions moving around with the finite-temperature MD run.

To summarize, we have developed a machine learning potential using the Gaussian Kernel Regression method, achieving accuracy comparable to ab-initio calculations. We use our model to perform molecular dynamics simulations on moiré unit cells of twisted *h*-BN containing on the order of  $10^4$  atoms, a scale previously unattainable using ab initio methods, while also providing improved

accuracy compared to standard classical potentials, even with applied uniaxial strain. The structural properties of the geometrically optimized structures obtained from our GAP model are consistent with the behavior of similar materials of the same class. Furthermore, we calculate the out-of-plane polarization of twisted *h*-BN using a tight-binding model based on interatomic distance-dependent hopping. Our results show excellent agreement with previous experimental results and improving upon the accuracy of previous ab-initio attempts. Since the polarization in twisted *h*-BN is of purely geometric

origin, we can confirm that our model performs accurately at small twist angle. Additionally, our model captures the effects of finite temperature and agrees with experimental results showing minimal change in polarization with temperature. This approach opens a door to more effectively study the effects of electric fields in the nanoscale regime.

## ACKNOWLEDGMENTS

This work was supported by the Research Foundation–Flanders (FWO–VI), Special Research Funds of the University of Antwerp (BOF-UA), and the FWO–FNRS EOS project ShapeME. The computational resources and services for this work were provided by the VSC (Flemish Supercomputer Center), funded by the FWO and the Flemish Government – department EWI.

- 
- [1] Y. Liu, Y. Huang, and X. Duan, Van der Waals integration before and beyond two-dimensional materials, *Nature* **567**, 323 (2019), publisher: Nature Publishing Group.
- [2] M. Vizner Stern, Y. Waschitz, W. Cao, I. Nevo, K. Watanabe, T. Taniguchi, E. Sela, M. Urbakh, O. Hod, and M. Ben Shalom, Interfacial ferroelectricity by van der Waals sliding, *Science* **372**, 1462 (2021), publisher: American Association for the Advancement of Science.
- [3] C. R. Woods, P. Ares, H. Nevison-Andrews, M. J. Holwill, R. Fabregas, F. Guinea, A. K. Geim, K. S. Novoselov, N. R. Walet, and L. Fumagalli, Charge-polarized interfacial superlattices in marginally twisted hexagonal boron nitride, *Nature Communications* **12**, 347 (2021), publisher: Nature Publishing Group.
- [4] T. Mikolajick, S. Slesazek, H. Mulaosmanovic, M. H. Park, S. Fichtner, P. D. Lomenzo, M. Hoffmann, and U. Schroeder, Next generation ferroelectric materials for semiconductor process integration and their applications, *Journal of Applied Physics* **129**, 100901 (2021).
- [5] R. Mears, W. Crossland, M. Dames, J. Collington, M. Parker, S. Warr, T. Wilkinson, and A. Davey, Telecommunications applications of ferroelectric liquid-crystal smart pixels, *IEEE Journal of Selected Topics in Quantum Electronics* **2**, 35 (1996), conference Name: IEEE Journal of Selected Topics in Quantum Electronics.
- [6] A. P. Sharma, M. K. Behera, D. K. Pradhan, S. K. Pradhan, C. E. Bonner, and M. Bahoura, Lead-free relaxor-ferroelectric thin films for energy harvesting from low-grade waste-heat, *Scientific reports* **11**, 111 (2021).
- [7] N. Higashitarumizu, H. Kawamoto, C.-J. Lee, B.-H. Lin, F.-H. Chu, I. Yonemori, T. Nishimura, K. Wakabayashi, W.-H. Chang, and K. Nagashio, Purely in-plane ferroelectricity in monolayer SnS at room temperature, *Nature communications* **11**, 2428 (2020).
- [8] J. A. Brehm, S. M. Neumayer, L. Tao, A. O’Hara, M. Chyasnachichus, M. A. Susner, M. A. McGuire, S. V. Kalinin, S. Jesse, P. Ganesh, S. T. Pantelides, P. Maksymovych, and N. Balke, Tunable quadruple-well ferroelectric van der Waals crystals, *Nature Materials* **19**, 43 (2020).
- [9] Y. Wu, Y. Zhang, X. Wang, W. Hu, S. Zhao, T. Officer, K. Luo, K. Tong, C. Du, L. Zhang, B. Li, Z. Zhuge, Z. Liang, M. Ma, A. Nie, D. Yu, J. He, Z. Liu, B. Xu, Y. Wang, Z. Zhao, and Y. Tian, Twisted-layer boron nitride ceramic with high deformability and strength, *Nature* **626**, 779 (2024), publisher: Nature Publishing Group.
- [10] J. O. Island, S. I. Blanter, M. Buscema, H. S. J. van der Zant, and A. Castellanos-Gomez, Gate Controlled Photocurrent Generation Mechanisms in High-Gain In<sub>2</sub>Se<sub>3</sub> Phototransistors, *Nano Letters* **15**, 7853 (2015), publisher: American Chemical Society.
- [11] S. Yuan, X. Luo, H. L. Chan, C. Xiao, Y. Dai, M. Xie, and J. Hao, Room-temperature ferroelectricity in MoTe<sub>2</sub> down to the atomic monolayer limit, *Nature Communications* **10**, 1775 (2019), publisher: Nature Publishing Group.
- [12] X. Zhang and B. Peng, The twisted two-dimensional ferroelectrics, *Journal of Semiconductors* **44**, 011002 (2023), publisher: Chinese Institute of Electronics.
- [13] R. R. Mehta, B. D. Silverman, and J. T. Jacobs, Depolarization fields in thin ferroelectric films, *Journal of Applied Physics* **44**, 3379 (1973).
- [14] D. Zhang, P. Schoenherr, P. Sharma, and J. Seidel, Ferroelectric order in van der Waals layered materials, *Nature Reviews Materials* **8**, 25 (2023).
- [15] K. Yasuda, X. Wang, K. Watanabe, T. Taniguchi, and P. Jarillo-Herrero, Stacking-engineered ferroelectricity in bilayer boron nitride, *Science* **372**, 1458 (2021), publisher: American Association for the Advancement of Science.
- [16] A. I. Khan, A. Keshavarzi, and S. Datta, The future of ferroelectric field-effect transistor technology, *Nature Electronics* **3**, 588 (2020), publisher: Nature Publishing Group.
- [17] J. Ding, H. Xiang, W. Zhou, N. Liu, Q. Chen, X. Fang, K. Wang, L. Wu, K. Watanabe, T. Taniguchi, N. Xin, and S. Xu, Engineering band structures of two-dimensional materials with remote moiré ferroelectricity, *Nature Communications* **15**, 9087 (2024), publisher: Nature Publishing Group.
- [18] S. Roux, J. Fraunié, K. Watanabe, T. Taniguchi, B. Lassigne, and C. Robert, Optical Detection of Sliding Ferroelectric Switching in hBN with a WSe<sub>2</sub> Monolayer, *Nano Letters* **25**, 321 (2025), publisher: American Chemical Society.
- [19] N. Tilak, M. Altvater, S.-H. Hung, C.-J. Won, G. Li, T. Kaleem, S.-W. Cheong, C.-H. Chung, H.-T. Jeng, and E. Y. Andrei, Proximity induced charge density wave in a graphene/1T-TaS<sub>2</sub> heterostructure, *Nature Communications* **15**, 8056 (2024), publisher: Nature Publishing Group.
- [20] M. Cho, B. Datta, K. Han, S. B. Chand, P. C. Adak, S. Yu, F. Li, K. Watanabe, T. Taniguchi, J. Hone, J. Jung, G. Grosso, Y. D. Kim, and V. M. Menon, Moiré Exciton Polaron Engineering via twisted hBN, *Nano Let-*

- ters **25**, 1381 (2025), publisher: American Chemical Society.
- [21] W. Aggoune, C. Cocchi, D. Nabok, K. Rezouali, M. A. Belkhir, and C. Draxl, Dimensionality of excitons in stacked van der Waals materials: The example of hexagonal boron nitride, *Physical Review B* **97**, 241114 (2018), publisher: American Physical Society.
- [22] P. Zhao, C. Xiao, and W. Yao, Universal superlattice potential for 2D materials from twisted interface inside h-BN substrate, *npj 2D Materials and Applications* **5**, 1 (2021), publisher: Nature Publishing Group.
- [23] V. L. Deringer, M. A. Caro, and G. Csányi, Machine Learning Interatomic Potentials as Emerging Tools for Materials Science, *Advanced Materials* **31**, 1902765 (2019), eprint: <https://onlinelibrary.wiley.com/doi/pdf/10.1002/adma.201902765>
- [24] Y. Zuo, C. Chen, X. Li, Z. Deng, Y. Chen, J. Behler, G. Csányi, A. V. Shapeev, A. P. Thompson, M. A. Wood, and S. P. Ong, Performance and Cost Assessment of Machine Learning Interatomic Potentials, *The Journal of Physical Chemistry. A* **124**, 731 (2020).
- [25] A. P. Bartók, R. Kondor, and G. Csányi, On representing chemical environments, *Physical Review B* **87**, 184115 (2013), publisher: American Physical Society.
- [26] V. L. Deringer, A. P. Bartók, N. Bernstein, D. M. Wilkins, M. Ceriotti, and G. Csányi, Gaussian Process Regression for Materials and Molecules, *Chemical Reviews* **121**, 10073 (2021), publisher: American Chemical Society.
- [27] P. Rowe, V. L. Deringer, P. Gasparotto, G. Csányi, and A. Michaelides, An accurate and transferable machine learning potential for carbon, *The Journal of Chemical Physics* **153**, 034702 (2020).
- [28] P. Rowe, G. Csányi, D. Alfè, and A. Michaelides, Development of a machine learning potential for graphene, *Physical Review B* **97**, 054303 (2018), publisher: American Physical Society.
- [29] F. L. Thiemann, P. Rowe, E. A. Müller, and A. Michaelides, Machine Learning Potential for Hexagonal Boron Nitride Applied to Thermally and Mechanically Induced Rippling, *The Journal of Physical Chemistry C* **124**, 22278 (2020), publisher: American Chemical Society.
- [30] T. Kocabaş, M. Keçeli, A. Vázquez-Mayagoitia, and C. Sevik, Gaussian approximation potentials for accurate thermal properties of two-dimensional materials, *Nanoscale* **15**, 8772 (2023), publisher: The Royal Society of Chemistry.
- [31] G. Kresse and J. Hafner, Ab initio molecular-dynamics simulation of the liquid-metal–amorphous-semiconductor transition in germanium, *Physical Review B* **49**, 14251 (1994), publisher: American Physical Society.
- [32] G. Kresse and J. Furthmüller, Efficient iterative schemes for ab initio total-energy calculations using a plane-wave basis set, *Physical Review B* **54**, 11169 (1996), publisher: American Physical Society.
- [33] C. Sevik, A. Kinacı, J. B. Haskins, and T. Çağın, Characterization of thermal transport in low-dimensional boron nitride nanostructures, *Physical Review B* **84**, 085409 (2011), publisher: American Physical Society.
- [34] C. Sevik, A. Kinacı, J. B. Haskins, and T. Çağın, Influence of disorder on thermal transport properties of boron nitride nanostructures, *Physical Review B* **86**, 075403 (2012), publisher: American Physical Society.
- [35] A. Kinacı, J. B. Haskins, C. Sevik, and T. Çağın, Thermal conductivity of BN-C nanostructures, *Physical Review B* **86**, 115410 (2012), publisher: American Physical Society.
- [36] W. Ouyang, D. Mandelli, M. Urbakh, and O. Hod, Nanoserpents: Graphene Nanoribbon Motion on Two-Dimensional Hexagonal Materials, *Nano Letters* **18**, 6009 (2018), publisher: American Chemical Society.
- [37] F. M. Arnold, A. Ghasemifard, A. Kuc, J. Kunstmann, and T. Heine, Relaxation effects in twisted bilayer molybdenum disulfide: structure, stability, and electronic properties, *2D Materials* **10**, 045010 (2023), arXiv:2306.07130 [cond-mat].
- [38] T. Latychevskaia, C. Escher, and H.-W. Fink, Moiré structures in twisted bilayer graphene studied by transmission electron microscopy, *Ultramicroscopy* **197**, 46 (2019).
- [39] W. Cao, O. Hod, and M. Urbakh, Interlayer Registry Dictates Interfacial 2D Material Ferroelectricity, *ACS Applied Materials & Interfaces* **14**, 57492 (2022), publisher: American Chemical Society.
- [40] N. A. Spaldin, A beginner’s guide to the modern theory of polarization, *Journal of Solid State Chemistry* **195**, 2 (2012), arXiv:1202.1831 [cond-mat].
- [41] D. S. Kim, R. C. Dominguez, R. Mayorga-Luna, D. Ye, J. Embley, T. Tan, Y. Ni, Z. Liu, M. Ford, F. Y. Gao, S. Arash, K. Watanabe, T. Taniguchi, S. Kim, C.-K. Shih, K. Lai, W. Yao, L. Yang, X. Li, and Y. Miyahara, Electrostatic moiré potential from twisted hexagonal boron nitride layers, *Nature Materials* **23**, 65 (2024), publisher: Nature Publishing Group.
- [42] R. Smeyers, M. V. Milošević, and L. Covaci, Strong gate-tunability of flat bands in bilayer graphene due to moiré encapsulation between hBN monolayers, *Nanoscale* **15**, 4561 (2023), publisher: The Royal Society of Chemistry.
- [43] P. Moon and M. Koshino, Electronic properties of graphene/hexagonal-boron-nitride moiré superlattice, *Physical Review B* **90**, 155406 (2014), publisher: American Physical Society.
- [44] D. Moldovan, Miša Anđelković, and Francois Peeters, py-binding v0.9.5: a Python package for tight-binding calculations (Zenodo, 2020) version Number: v0.9.5.
- [45] A. Weiße, G. Wellein, A. Alvermann, and H. Fehske, The kernel polynomial method, *Reviews of Modern Physics* **78**, 275 (2006), publisher: American Physical Society.
- [46] N. R. Walet and F. Guinea, Flat bands, strains, and charge distribution in twisted-bilayer hBN, *Physical Review B* **103**, 125427 (2021), arXiv:2011.14237 [cond-mat].
- [47] D. Bennett, G. Chaudhary, R.-J. Slager, E. Bousquet, and P. Ghosez, Polar meron-antimeron networks in strained and twisted bilayers, *Nature Communications* **14**, 1629 (2023), arXiv:2210.10786 [cond-mat].
- [48] J. P. Perdew, K. Burke, and M. Ernzerhof, Generalized Gradient Approximation Made Simple, *Physical Review Letters* **77**, 3865 (1996), publisher: American Physical Society.
- [49] S. Grimme, J. Antony, S. Ehrlich, and H. Krieg, A consistent and accurate ab initio parametrization of density functional dispersion correction (DFT-D) for the 94 elements H-Pu, *The Journal of Chemical Physics* **132**, 154104 (2010).
- [50] S. Grimme, S. Ehrlich, and L. Goerigk, Effect of the damping function in dispersion corrected density functional theory, *Journal of Com-*



- putational Chemistry **32**, 1456 (2011), eprint: <https://onlinelibrary.wiley.com/doi/pdf/10.1002/jcc.21759>.
- [51] P. E. Blöchl, Projector augmented-wave method, *Physical Review B* **50**, 17953 (1994), publisher: American Physical Society.
- [52] G. Kresse and D. Joubert, From ultrasoft pseudopotentials to the projector augmented-wave method, *Physical Review B* **59**, 1758 (1999), publisher: American Physical Society.
- [53] H. J. Monkhorst and J. D. Pack, Special points for Brillouin-zone integrations, *Physical Review B* **13**, 5188 (1976), publisher: American Physical Society.
- [54] R. W. Lynch and H. G. Drickamer, Effect of High Pressure on the Lattice Parameters of Diamond, Graphite, and Hexagonal Boron Nitride, *The Journal of Chemical Physics* **44**, 181 (1966).
- [55] S. Naik, M. H. Naik, I. Maity, and M. Jain, Twister: Construction and structural relaxation of commensurate moiré superlattices, *Computer Physics Communications* **271**, 108184 (2022), arXiv:2102.07884 [cond-mat].
- [56] M. H. Naik and M. Jain, Ultraflatbands and Shear Solitons in Moiré Patterns of Twisted Bilayer Transition Metal Dichalcogenides, *Physical Review Letters* **121**, 266401 (2018), publisher: American Physical Society.
- [57] V. Pal and Ajay, Twist angle, strain, corrugation and moire unit cell in twisted bi-layer graphene, *Modelling and Simulation in Materials Science and Engineering* **32**, 035013 (2024), publisher: IOP Publishing.
- [58] A. P. Bartók, M. C. Payne, R. Kondor, and G. Csányi, Gaussian Approximation Potentials: The Accuracy of Quantum Mechanics, without the Electrons, *Physical Review Letters* **104**, 136403 (2010), publisher: American Physical Society.
- [59] S. Klawohn, J. P. Darby, J. R. Kermode, G. Csányi, M. A. Caro, and A. P. Bartók, Gaussian approximation potentials: Theory, software implementation and application examples, *The Journal of Chemical Physics* **159**, 174108 (2023).
- [60] S. Javvaji, F. Li, and J. Jung, Ab initio tight-binding models for mono- and bilayer hexagonal boron nitride (h-BN), *Physical Review Materials* **9**, 024004 (2025), publisher: American Physical Society.
- [61] J. C. Slater and G. F. Koster, Simplified LCAO Method for the Periodic Potential Problem, *Physical Review* **94**, 1498 (1954), publisher: American Physical Society.

tials [51, 52] were also employed. We chose the PBE+D3 correction because it was successfully used in a previous GAP potential for hBN in several phases [29], and also it has proven successful in predicting lattice parameter of bulk hBN. The reciprocal lattice was sampled in the Monkhorst-Pack grid [53] with a maximum distance between the k-points of  $0.02 \text{ \AA}^{-1}$ .

Before generating the twisted structures to perform AIMD on them, we have to find the appropriate interlayer distance according to the settings of our simulation, this is shown in figure 5. For the lattice constant we take the established value for hBN from previous works[54]. After establishing these values, we proceeded and generated twisted structures of hBN using the Twister python package [55, 56], creating bilayer hBN twisted structures from  $0.91^\circ$  to  $21.78^\circ$ , all according to the definition of commensurate unit cells[57].

To construct the data base, we followed a similar procedure as the one described in [28], in which we build the training set using an iterative approach. We started with an AIMD run at 100 K for angles of  $21.78^\circ$ ,  $13.17^\circ$ ,  $9.43^\circ$  and  $7.34^\circ$ , running these for at least 1000 fs to obtain enough samples of the configuration space. From all these configurations, we choose 1000 configurations to train the first version of our GAP based on the energies and forces for each atom. With this first version of our potential we generate different MD trajectories at 100 K, 200 K and 300 K, and do a single point energy calculation to obtain energies and forces from each individual atom. We proceed to train once again a different version of the GAP and repeat this process iteratively until we achieve the desired accuracy. The last training set contained 1300 different configurations of MD trajectories and relaxation trajectories, and from this we chose 20% of them for a test set.

## Appendix A: I. Generation of Training Set

The accuracy of the potential depends on the robustness of the training set. In this purpose, we generated our training set based on ab-initio molecular dynamics(AIMD) using a Density Functional Theory (DFT) code as implemented in the Vienna Ab initio Simulation Package (VASP) [31, 32]. In the following, all the ab-initio calculations were performed using the VASP plane-wave DFT code employing the Perdew-Burke-Ernzerhof (PBE)[48] functional with the DFT-D3 dispersion correction method [49] using the Becke-Johnson damping [50], an energy cut-off of 620 eV, a Gaussian smearing of 0.05 eV, and projector augmented wave pseudopotentials

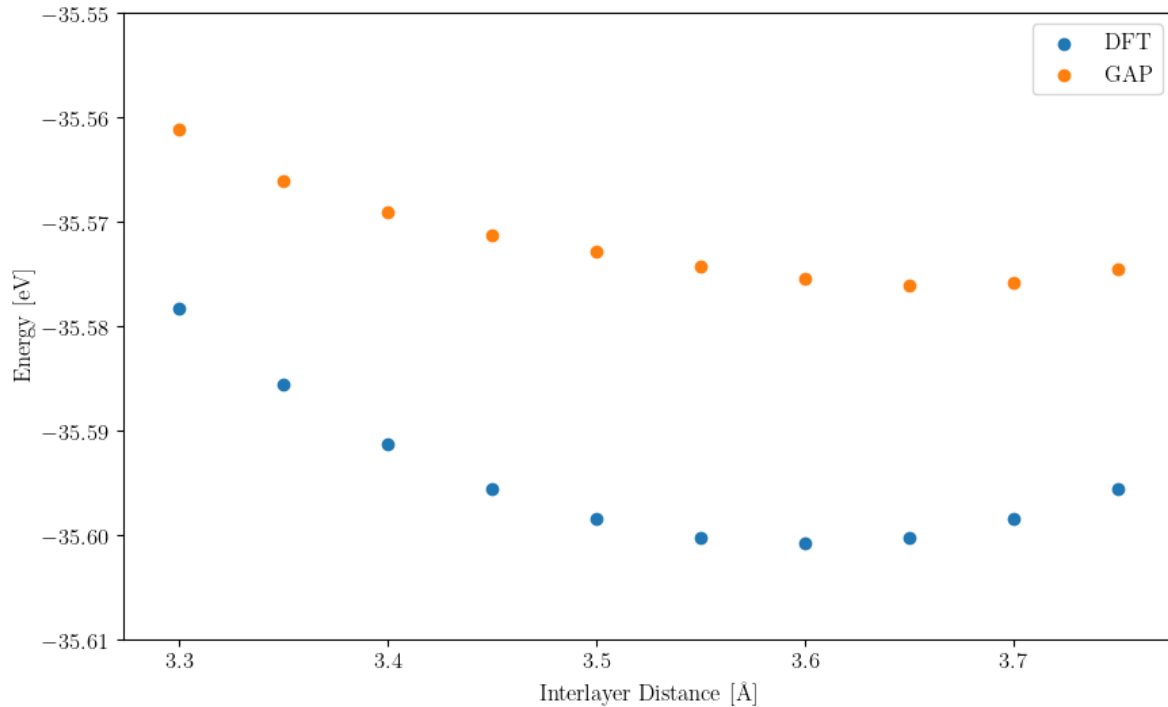


Figure 5. Equation of state for bilayer  $h$ -BN in AA stacking including the comparison with the prediction of our GAP potential.

## Appendix B: II. Gaussian Approximation Potential

Gaussian Approximation Potential (GAP) was proposed as a solution to the problem of interpolating the Born-Oppenheimer potential energy surface (PES) of a system via the application of the Gaussian kernel regression machine learning methodology [58]. The advantage of GAP over previous empirical potentials is that it does not assume a functional form into which the PES has to be decomposed. From the ab-initio dataset, GAP has only available the energies, forces and virial stresses of the system, so in that sense, to facilitate systems with larger sizes, GAP decomposes the atomic environment into a sum of local contributions. These contributions are then computed via kernel functions which represent the similarity between chemical environments. Usually we decompose the contributions into two body, three body, or many body interactions, specifically for this work we decided to represent every contribution with many body interactions.

The many body interaction takes the form of the smooth overlap of atomic positions (SOAP) descriptor, within this descriptor, each atomic environment is described by a local density of neighbors, generated by summing over Gaussians that are placed in each atom within a specific cut-off. The density for the  $i$ th atom is expanded in a basis of radial functions and spherical

harmonics:

$$\rho_i(\mathbf{r}) = \sum_{\substack{n < n_{max} \\ l < l_{max} \\ |m| \leq l}} c_{nlm}^i g_n(r) Y_{lm}(\mathbf{r}) \quad (\text{B1})$$

wherein the power spectrum of the coefficients  $c_{nlm}^i$  form the SOAP vectors. It is worth mentioning that these SOAP descriptors are invariant under rotations, which becomes relevant for our system of study.

In addition to the descriptor, there are several other hyperparameters that impact the performance and accuracy of a GAP potential; in this work we will only focus on the most important ones, for a more detailed discussion about GAP descriptors and hyperparameters, consult elsewhere [59]. Due to the flexibility of its descriptors and hyperparameters, GAP is the most promising ML potential to reproduce the vdW interaction in layered heterostructures of 2D materials. GAP also has the clear advantage of low computational cost with respect to ab-initio methods, which is critical when dealing with a large number of atoms (such as in so-called moiré heterostructures, where periodic unit cells become very large due to lattice mismatch or twist between the constituent monolayers). In table I the relevant hyperparameters are shown, we chose a bigger cut-off than the one from the previous GAP potential for hBN in order to also include

SOAP descriptor	
cut-off [ $\text{\AA}$ ]	6.0
cut-off width [ $\text{\AA}$ ]	1.0
$\delta$ [eV]	0.2
sparse method	CUR
sparse points	1100
$l_{max}$	6
$n_{max}$	6
$\zeta$	2
target deviations	
$\sigma_{energy}$	0.005
$\sigma_{force}$	0.0005
$\sigma_{virial}$	0.005

Table I. Model parameters for the twisted bilayer hBN GAP.

the interlayer interaction in this descriptor, and in this way discard the use of another descriptor to reproduce different interactions. Due to the trade-off between computational cost and accuracy of the model, we decided to truncate the spherical harmonics of the SOAP descriptor after the 6th order, this has proven to be enough to reach the desired accuracy. Instead of using all of the local environments of the training set, a covariance matrix is constructed based on 1100 points, this will focus the model to train on specific parts of the training configuration space. The target deviations assign the fit and the weight between the values predicted from the model to the target values in the training configuration.

### Appendix C: III. Tight Binding Model

We describe the system with a tight-binding model that uses Bloch wave functions of the form

$$|\Psi_{\mathbf{k}}\rangle = \frac{1}{\sqrt{N}} \sum_i^N e^{i\mathbf{k}\mathbf{R}_i} |\phi_i\rangle \quad (\text{C1})$$

where  $|\phi_i\rangle$  describes the wavefunction of atomic site  $i$  at position  $\mathbf{R}_i$ . The general form of the tight-binding Hamiltonian is

$$H = - \sum_{i,j} t(\mathbf{R}_i - \mathbf{R}_j) |\phi_i\rangle \langle \phi_j| + \sum_i V(\mathbf{R}_i) |\phi_i\rangle \langle \phi_i| \quad (\text{C2})$$

In the Hamiltonian from eq. C2, the first term defines the hopping between sites  $i$  and  $j$  with strength  $t$ . The second term represents the on-site potential, in which we used  $V_B = -1.287$  eV and  $V_N = -5.393$  eV, values obtained from [60]. We used the Slater-Koster type of functions [61], which give a good estimate of the hopping value depending on the relative positions between atomic orbitals. Following the procedures from [43] we get to the following expression for the distance depending hopping:

$$t(r_{ij}) = \left( \frac{z_{ij}}{r_{ij}} \right)^2 V_{pp\sigma}(r_{ij}) + \left( 1 - \left( \frac{z_{ij}}{r_{ij}} \right)^2 \right) V_{pp\pi}(r_{ij}) \quad (\text{C3})$$

where  $z_{ij}$  is the component of  $r_{ij}$  along the z-axis. We also define

$$V_{pp\sigma}(r_{ij}) = \gamma_1 \exp\left(q_\sigma \left(1 - \frac{r_{ij}}{c}\right)\right) \quad (\text{C4a})$$

$$V_{pp\pi}(r_{ij}) = \gamma_0 \exp\left(q_\pi \left(1 - \frac{r_{ij}}{a_{BN}}\right)\right) \quad (\text{C4b})$$

$$\frac{q_\sigma}{c} = \frac{q_\pi}{a_{BN}} = \frac{\ln(\gamma'_0/\gamma_0)}{a_{BN} - a} \quad (\text{C4c})$$

where  $\gamma_0$  is the nearest neighbor interaction (-2.7 eV),  $\gamma'_0$  is the next nearest neighbor interaction ( $0.1\gamma_0$ ),  $c$  parameter is the interlayer distance in the AA stacking, and  $a$  is the optimized lattice parameter. We have to define specific hopping parameter prefactors depending on the atomic species, so we defined them as

$$\gamma_{BB,1} = 0.831\text{eV} \quad (\text{C5a})$$

$$\gamma_{NN,1} = 0.3989\text{eV} \quad (\text{C5b})$$

$$\gamma_{BN,1} = 0.6601\text{eV} \quad (\text{C5c})$$